Analysis of Low-Energy-Electron Diffraction Intensity Profiles from the (100) and (111) Faces of Nickel*

G. E. Laramore
Sandia Laboratories, Albuquerque, New Mexico 87115
(Received 12 February 1973)

Low-energy-electron-diffraction (LEED) intensity profiles are calculated for the (100) and (111) faces of nickel and compared with experimental measurements. An electron–ion-core potential of the conventional muffin-tin form is used in this work. The inner potential V_0 is determined from work-function measurements using the position of the d-wave resonance to locate the approximate (within 1-2 eV) position of the Fermi level. This value of V_0 gives a good placement of peak positions for electron energies ≤ 240 eV for both faces. A constant mean-free-path parameter of $\lambda_{ee}=8$ Å is used to parametrize the imaginary part of the one-electron proper self-energy. Five partial-wave components are used to describe the vibronically renormalized electron–ion-core elastic-scattering vertex. The results adequately describe both the absolute intensities and the shapes of the experimental intensity profiles for the (100) face but only the shapes of the experimental intensity profiles for the (111) face. Analysis of the data indicates that the upper layer spacing is the same as the bulk value (to within ~ 0.1 Å) for both faces.

I. INTRODUCTION

In this paper the finite-temperature version of the inelastic collision model[1–4] is used to analyze experimental[5–9] low-energy-electron-diffraction (LEED) intensity profiles from the (100) and (111) faces of nickel. The experimental data considered here cover the energy range between 0 and 240 eV for a reasonable range of angles of incidence. The published data for the (110) face[7] are considerably more limited and so the (110) face is not included in the present study. Phase shifts from a conventional muffin-tin "band-structure" potential are used to describe the electron–ion-core interaction. Thus, this work contrasts with a previous study[6] of nickel which analyzes a substantially smaller amount of data using a potential with the exchange component especially modified[10] for the relatively high-energy range of LEED. The present work shows that the band-structure potential satisfactorily describes the experimental data and, along with other LEED calculations[11–16] using band-structure potentials, argues against Pendry's assertion[10] that the exchange approximations used in constructing potentials for energy-band calculations are not suitable for the higher-energy range of LEED. The inner potential V_0 is determined from work-function measurements[17] using the d-wave resonance to locate the approximate (within 1–2 eV) position of the Fermi level. In materials such as transition metals, where the Fermi level lies within a *narrow* partially filled band, this approach provides a way of independently fixing V_0 without resorting to a full band-structure calculation. This value of V_0 agrees well with that obtained by comparing calculated intensity profiles with the normal-incidence measurements of Andersson and Kasemo.[5] It gives a good placement of peak positions for electron energies $\lesssim 240$ eV for both faces. Previous work on LiF also showed that a value of V_0 consistent with the absolute location of the low-lying electronic bands relative to the vacuum gave a good description of the LEED data.[15]

Five partial-wave components are used to describe the electron–ion-core elastic scattering vertex. The renormalization due to the lattice vibrations is parametrized using the bulk Debye temperature[18] of 440 °K. The imaginary part of the electronic proper self-energy is parametrized in terms of a constant inelastic mean free path as was originally done by Duke and Tucker.[19] The calculations adequately describe *both* the absolute intensities and the shapes of the experimental intensity profiles[5,6] for Ni(100) at $T=300$ °K. On Ni(111) the only available absolute intensity measurements[8,9] are at $T=423$ °K, and although the model calculations provide an adequate description of the shapes of the experimental intensity profiles, they are off by almost an order of magnitude with respect to the absolute intensities. Taking account of a larger amplitude of the surface atoms (relative to those in the bulk) does not completely remedy this difficulty. The dependence of the calculated intensity profiles on small changes in the upper layer spacing is investigated for the specular beam at near normal incidence. Analysis of the data indicates that the upper layer spacing is the same as the bulk value (to within ~ 0.1 Å) for both faces. This contrasts with the conclusion of MacRae and Germer[20] that the upper layer spacing of Ni(111) was expanded by 5% relative to its bulk value. Their conclusion was based upon an argument regarding peak shifts relative to kinematical Bragg positions. While a charge in the upper layer spacing does produce such peak shifts,[21] multiple scattering effects from a strong potential

can also shift peaks relative to their kinematical Bragg positions.

The details of the model calculations differ slightly from previous work[3,15] and these differences are set forth in Sec. II. In Sec. III we describe the electron–ion-core potential used in the model calculations and show that the value of the inner potential obtained from work-function measurements agrees with that obtained by fitting the calculated intensity profiles to Andersson and Kasemo's experimental measurements.[5] Model calculations of LEED intensity profiles are compared with experimental measurements for Ni(100) in Sec. IV and for Ni(111) in Sec. V. Finally, in Sec. VI we summarize our results.

II. DESCRIPTION OF MODEL

The basic equations that relate the partial-wave components of the vibronically renormalized electron–ion-core elastic scattering vertices to the reflectivity of a given beam have been previously set forth by Laramore and Duke.[2,3] Here we only detail the ways in which the present calculation differs from previous work.[2,3,15]

First, real analogs of the spherical harmonics are used in the various partial-wave expansions rather than the complex forms used before. The particular basis set used is

$$\tilde{Y}_{l,m}(\Omega) = (-i/\sqrt{2})[Y_{l,m}(\Omega) - (-1)^m Y_{l,m}(\Omega)] , \tag{1a}$$

$$\tilde{Y}_{l,-m}(\Omega) = (1/\sqrt{2})[Y_{l,m}(\Omega) + (-1)^m Y_{l,m}] , \tag{1b}$$

where $m > 0$ and

$$\tilde{Y}_{l,0}(\Omega) = Y_{l,0}(\Omega) . \tag{2}$$

The $Y_{l,m}(\Omega)$ are the usual complex forms.[22] With these definitions, the basic form of the equations given in Refs. 2 and 3 remain unchanged although the numerical values of the coupling coefficients occurring in the definition of the structural Green's functions are altered. The advantage of the change of basis is that the structural Green's functions are symmetric in the angular momentum indices [as are the scattering amplitudes $\tau_\lambda^{LL'}(k(E))$ and $T_\lambda^{LL'}(k(E))$] and this simplifies the generation and storage of the various quantities.

The question of various possible boundary conditions on the scattered beams has been raised by Duke *et al.*[16] In the absence of reflection at the potential barrier between the solid and the vacuum it is generally agreed that when the momentum dependence of the electronic self-energy can be neglected, the reflection *amplitude* associated with the gth beam can be written[3,16,23,24]

$$R(\vec{g}, E) = \frac{-mi R_g(\vec{k}_f, \vec{k}_i)}{k^2 A \vec{k}_\perp(\vec{g}, E)} , \tag{3}$$

where $\vec{k}_{f\parallel} = \vec{k}_{i\parallel} + \vec{g}$ and

$$R_g(\vec{k}_f, \vec{k}_i) = \sum_\lambda \exp[-i(k_{f\perp} - k_{i\perp})d_\lambda - i\vec{g}\cdot\vec{a}_\lambda] T_\lambda(\vec{k}_f, \vec{k}_i) . \tag{4}$$

In Eq. (4) T_λ is the sum of all scattering processes where the final scattering event takes place in the λth subplane which has its origin at $(\vec{a}_\lambda, d_\lambda \hat{z})$ [see Ref. 3 for a definition of the remaining quantities in Eqs. (3) and (4)]. T_λ is calculated in terms of its partial-wave components

$$T_\lambda(\vec{k}_f, \vec{k}_i) = \sum_{LL'} T_\lambda^{LL'}(k(E)) \tilde{Y}_L(\hat{k}_f) \tilde{Y}'_L(\hat{k}_i) , \tag{5}$$

where $\tilde{Y}_L(\hat{k})$ means that the spherical harmonics are written as functions of the wave vector $\vec{k}$ [i.e., $k_\perp$, $\vec{k}_\parallel$, and $k(E)$]. There is some question about the proper way of doing this since $k_\perp$ and $k(E)$ are complex.[16] Physically, the complex nature of the wave vectors comes about because of inelastic processes that cause the elastic beam to attenuate as it passes through the solid. For this decay to occur both as the electron beam propagates to layer λ and then from layer λ back out to the surface, then in Eq. (4) $k_{i\perp}$ must lie in the first quadrant and $k_{f\perp}$ must lie in the third quadrant in the complex plane. (Note that the solid has been assumed to occupy the half-space $z \geq 0$ with $\vec{k}_i$ describing propagation into the solid and $\vec{k}_f$ describing propagation out of the solid.) For consistency, these $k_\perp$'s are used in defining the spherical harmonics used in Eq. (5). That is, the $\tilde{Y}_L$'s are written in terms of a real wave vector $\vec{S}$ and then the replacements

$$|\vec{S}| \to k(E), \qquad \vec{S}_\parallel \to \vec{k}_\parallel, \qquad S_\perp \to k_\perp \tag{6}$$

are made, with the conventions for $k_{i\perp}$ and $k_{f\perp}$ stated above. Exactly the same procedure was used previously[2,3,15,25,26] with the complex Y_L's, with the additional stipulation that the process of complex conjugation was done before the real wave vectors were replaced with their complex counterparts. The present procedure with the real $\tilde{Y}_L$'s is numerically the same as the previous prescription. This procedure is a natural outgrowth of the definitions of the Y_L's that are used in a perturbation calculation of T_λ, where one must take proper account of $k_\perp$ to ensure damping during the intermediate propagation stages.[2,23]

The second way this calculation differs from previous work is in the algorithm used to calculate the renormalization of the electron–ion-core elastic scattering vertex due to the lattice vibrations. Assuming a spherically symmetric mode of vibration, we can write[1,2] the effective electron–ion-core elastic scattering vertex for the nth ion core

$$b_n(\vec{k}_2, \vec{k}_1) = \exp[-W(T, \Theta_D^n, M_n)$$

$$\times(\vec{k}_2-\vec{k}_1)^2]\,t_n(\vec{k}_2,\vec{k}_1)\,, \quad (7)$$

where

$$W(T,\Theta_D^n,M_n)=\frac{3\hbar^2}{2M_n k_B\Theta_D^n}\times\left[\frac{1}{4}+\left(\frac{T}{\Theta_D^n}\right)^2\int_0^{\Theta_D^n/T}dx\,\frac{x}{e^x-1}\right] \quad (8)$$

and $t_n(\vec{k}_2,\vec{k}_1)$ is the scattering amplitude for the ion core when it is held rigid. In Eq. (8) T is the temperature of the solid, M_n is the mass of the nth ion core, and Θ_D^n is the Debye temperature parammetrizing the vibrational amplitude of the ion core.

Previously, Eq. (7) was evaluated by making a partial-wave expansion of $t_n(\vec{k}_2,\vec{k}_1)$ (keeping a specified number of terms) and then *directly* calculating the terms in the partial-wave expansion for $b_n(\vec{k}_2,\vec{k}_1)$. This procedure is described in detail in Ref. 3. However, for a given number of terms in the partial-wave expansion, the behavior of the vibronic renormalization factor can be more accurately modeled by writing it as

$$e^{-(\vec{k}_2-\vec{k}_1)^2W}\simeq e^{-2k^2W}\sum_{l=0}^{m}A_l(k,W)P_l(\cos\theta_{12})\,, \quad (9)$$

where $W=W(T,\Theta_D^n,M_n)$, $k=|\vec{k}_1|=|\vec{k}_2|$, and θ_{12} is the angle between $\vec{k}_1$ and $\vec{k}_2$. The A_l's are determined by equating the left- and right-hand sides of Eq. (9) at m judiciously chosen values of θ_{12}. Here we restrict ourselves to three terms in the expansion and fit the coefficients at $\theta_{12}=0$, $\frac{1}{2}\pi$, and π. An example of the accuracy that can be obtained via this procedure is shown in Fig. 1 of Ref. 25. For the heavier mass and larger Θ_D of nickel, the fit is even more precise. Explicit expressions for A_0, A_1, and A_2 are given in Ref. 25. The coefficients in the partial-wave expansion of $b_n(\vec{k}_2,\vec{k}_1)$ are obtained by straightforwardly writing

$$\begin{aligned}b_n(k_2,k_1)&=e^{-2k^2W}\sum_{l''=0}^{2}A_{l''}(W,k)P_{l''}(\cos\theta_{12})\\&\quad\times\sum_{l''=0}^{\bar{l}}\frac{2l''+1}{4\pi}\,t_{l''}(k)P_{l''}(\cos\theta_{12})\\&=\sum_{l=0}^{\bar{\bar{l}}}\frac{2l+1}{4\pi}\,b_l(k)P_l(\cos\theta_{12})\,,\end{aligned} \quad (10)$$

and solving for the $b_l(k)$ using the orthogonality relationship of the Legendre polynomials. In the current work five partial-wave components are used taking $\bar{l}=\bar{\bar{l}}=4$. The t_l's are defined in terms of partial-wave phase shifts from the electron–ion-core potential as given in Ref. 3.

The same simple model for the electronic self-energy used in previous works[1-3,15,19,25,26] is used here, i.e.,

$$\Sigma(\vec{k},E)=\Sigma(E)=-V_0-i\Gamma(E)\,, \quad (11)$$

where

$$\Gamma(E)=\frac{\hbar^2}{m\lambda_{ee}}\left(\frac{2m}{\hbar^2}(E+V_0)\right)^{1/2} \quad (12)$$

and V_0 is taken to be the distance from the muffin-tin zero to the vacuum. This is determined from work-function measurements as described in Sec. III. However, unlike previous works, the renormalization effects of the electronic self-energy are assumed to start one-half of an atomic layer spacing outside the position of the outermost plane of ion cores. This corresponds to taking $d_0=\frac{1}{2}d$ in Eq. (4), where d is the bulk layer spacing [$d=1.76$ Å for the (100) surface and 2.032 Å for the (111) surface at 300 °K]. Such an extension of the self-energy renormalization effects has been used by others[5,11-14,23] with the idea that it helps to take account of the extension of the conduction electrons beyond the position of the outermost plane of ion cores. It also may help to account phenomenologically for energy losses due to coupling to the surface plasmons while the electron is still "outside" the solid.[16,27] A value of $\lambda_{ee}=8$ Å seems to provide a reasonable description of the experimental data. Five atomic layers are considered in the calculations shown in this paper.

Finally, in this work we define the nonspecular beams for both the (100) and (111) faces in terms of the primitive two-dimensional surface cell as indicated in Fig. 1. The azimuthal angle ϕ is defined relative to the (10) direction as indicated in the figure. The angles and beams of the various experimental works will be translated into this notation. This seems preferable to defining the beams for the (100) face of an fcc material in terms of the nonprimitive cubic axes lying in the plane and the beams for the (110) and (111) surfaces of the same systems in terms of the primitive two-dimensional cell of the surface.[28]

III. ELECTRON-ION-CORE MODEL POTENTIAL

The electron–ion-core potential used in this work was obtained using conventional band-structure techniques. Atomic charge densities were obtained following the relativistic Hartree–Fock–Slater calculation of Liberman *et al.*[29] These atomic charge densities were overlapped and a muffin-tin potential constructed following Loucks.[30] The Slater[31] local-exchange approximation

$$V_{\text{exch}}(r)=-6\alpha[\tfrac{3}{8}\pi\rho(r)]^{1/3} \quad (13)$$

was used with the Kohn-Sham[32] value of $\alpha=\frac{2}{3}$ in both the free-atom calculations and the muffin-tin construction. A three-dimensional perfect crystal configuration was assumed in the potential construction with a lattice constant of 3.52 Å and a muffin-tin radius of 1.24 Å being used. This approach can be modified for surface atoms by appropriately changing the atomic coordination num-

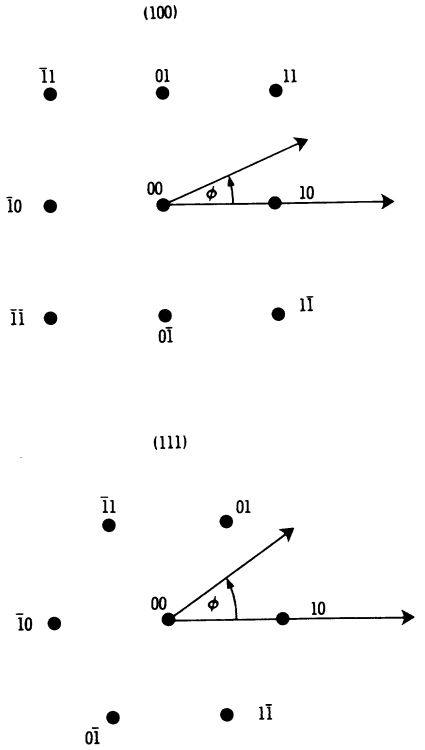

FIG. 1. Schematic illustration of the beam indexing for the (100) and (111) surfaces of an fcc material. The indexing is defined using the two-dimensional primitive cell of the surface. The azimuthal angle ϕ is defined relative to the (10) direction for a normally incident beam. The particular primitive cell used for the (111) face is in accord with Jona (Ref. 28).

bers.[16,33] The resulting potentials for the surface atoms have been successfully used to describe the shift of the core levels of the surface atoms relative to their bulk counterparts,[33] which indicates that this procedure is valid. However, the use of the resulting surface potentials appears to have little effect (for clean metal surfaces) on the calculated LEED intensity profiles.[16]

The $l = 0$–4 phase shifts obtained from this potential are shown in Fig. 2. The value of V_0, the distance of the muffin-tin zero from the vacuum, was calculated as 18.4 eV. However, the energy bands calculated using this value of V_0 would not give a Fermi level consistent with work-function measurements.[17] Notice in Fig. 2 that the sharp d-wave resonance occurs at ~ 9 eV above the muffin-tin zero. The position of this resonance locates the approximate position of the center of gravity of the d band.[34,35] Since the d bands of transition metals are fairly narrow and since the Fermi level of Ni lies within the d band, we know it is located within 1–2 eV of the d-wave resonance. Using $V_0 = 18.4$ eV would place the Fermi level ~ 9.4 eV below the vacuum resulting in a calculated work function of $\phi \sim 9.4$ eV. However, the measured work function[17] (polycrystalline Ni) is 5 eV and the variation of it from face to face is only about[36] ~ 0.5 eV. Thus, to be consistent with the work-function measurement, we should use $V_0 = 14$ eV. This approach of treating V_0 as an adjustable parameter is common in band-structure calculations since changing it merely gives a rigid shift of the bands.

Jepsen and co-workers[11–14] obtain V_0 directly from the LEED measurements. In Fig. 3 we show that this approach also indicates that the calculated value of V_0 is about 4–6 eV too large. In Fig. 3 calculated intensity profiles using $V_0 = 18.4$ eV for Ni(100) at normal incidence are compared with the experimental measurements of Andersson and Kasemo.[5] The shaded areas indicate the offset in energy between corresponding peaks in the intensity profiles. Since the comparison is for normal incidence [for the (100) beam the experimental curve is actually for $\theta \sim 1°$, $\phi = 45°$], the offsets give a good measure of the necessary correction to V_0. In general, these numbers agree quite well with the change of 4.4 eV obtained from the work-function data. Both the theoretical and experimental curves are for the absolute reflectivity. Note the good agreement between theory and experiment both in the shapes of the peaks and their absolute intensities. The threshold behavior of the (10) beam is not satisfactorily described by the calculation, but in Sec. IV we shall see that this is remedied when the calculation is redone using $V_0 = 14$ eV.

Treating V_0 as an adjustable parameter is not completely satisfactory from a theoretical viewpoint. However, it appears that this adjustment can be made via a band-structure calculation to locate either the Fermi level in metals or the top of the valence band in insulators and then appealing to either work-function measurements or photo-

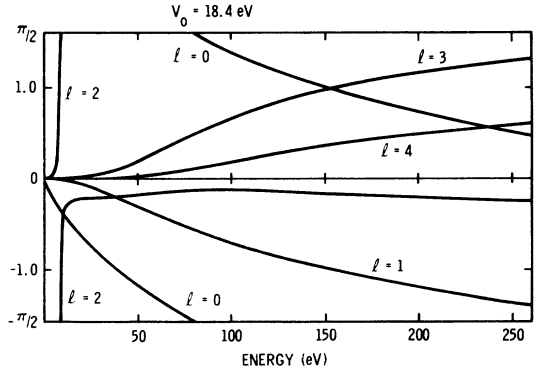

FIG. 2. Nickel phase shifts from the muffin-tin potential described in the text. The energy scale is measured relative to the constant value of the potential between the muffin tins. This zero level was calculated to be 18.4 eV below the vacuum.

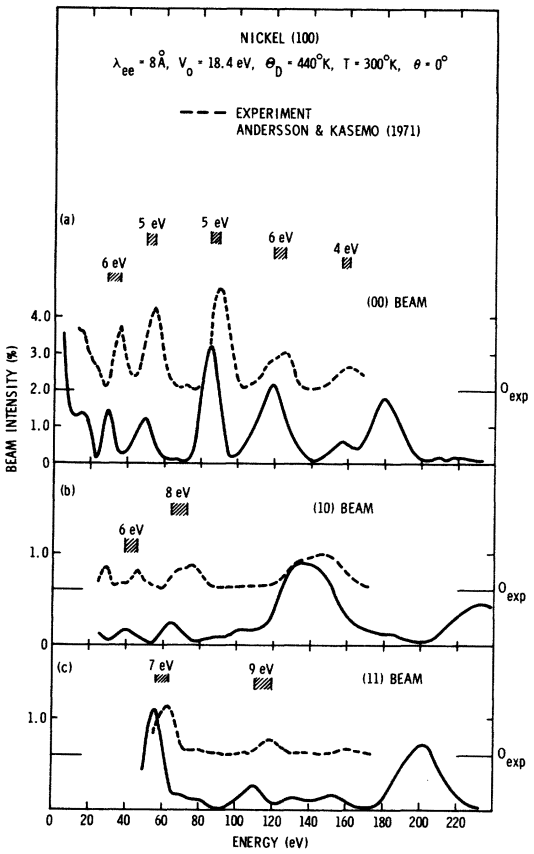

FIG. 3. Comparison between the predictions of the model calculations using $V_0 = 18.4$ eV and the experimental measurements of Andersson and Kasemo (Ref. 5) for (a) the specular beam, (b) the (10) beam, and (c) the (11) beam. Both the theoretical and the experimental curves are for the absolute reflectivities. The experimental zero levels have been shifted to the 2% mark for the (00) beam and to the 0.6% mark for the (10) and (11) beams. The shaded areas indicate the offset between corresponding peaks in the theoretical and experimental curves. The parameters used in the calculation are given in the figure. The experimental nonspecular beams are at $\theta = 0°$, but the experimental specular beam is for $\theta \sim 1°$, $\phi = 45°$.

emission data. As can be seen in Fig. 3, this value of V_0 appears relatively constant over a rather large energy range. This fact, observed several times before,[3,11,15] is in marked contrast with the large energy variation found in current electron-gas calculations of the real part of the one-electron self-energy.[37] As we have seen here, this determination of V_0 can sometimes be made without recourse to a full band-structure calculation if a key level can be determined (approximately) from the position of a partial-wave resonance. The value $V_0 = 14$ eV will be used in the remainder of the calculations presented in this paper. This is 5 eV smaller than the value of $V_0 = 19$ eV quoted by Andersson and Pendry[38] as giving the best fit to the same experimental data using a potential constructed according to Pendry's prescription.[10] The phase shifts used in the present work differ appreciably[39] from those obtained via Pendry's prescription and this presumably is the origin of the different "best-fit" values of V_0.

IV. NICKEL (100)

In this section we compare calculated intensity profiles for Ni(100) with experimental measurements. Since once the $T_\lambda^{LL'}$ have been obtained for a given angle of incidence, it costs little additional computer time to calculate the intensities of several "extra" beams as well [see Eqs. (4) and (5)], we will also show some calculated intensity profiles for some beams that have not been measured as yet. It is hoped that this will motivate additional experimental work and provide a more accurate test of the theoretical model. Unless otherwise stated, the calculations in this section treat the surface as though it were simply a truncation of an idealized perfectly periodic bulk solid. The 300 °K lattice constant (3.52 Å) is used.

In Fig. 4 we show a comparison between the calculated intensity profiles for a normally incident beam and the experimental measurements of Andersson and Kasemo.[5] There is reasonable agreement between theory and experiment with respect to both the shapes and positioning of the various peaks and their absolute intensities. The calculations and the experimental measurements are at room temperature ($T \sim 300$ °K). Note the improved description of the threshold behavior of the (10) beam compared with that shown in Fig. 3. Threshold behavior can be fairly sensitive to the value of V_0 used in the calculation.

A comparison between the calculated intensity profile for the (100) beam at $\theta = 5°$, $\phi = 45°$ and the experimental data of Andersson and Kasemo[5] and of Demuth *et al.*[6] is shown in Fig. 5. Calculated curves for the $(0\bar{1})$ and $(\bar{1}\,\bar{1})$ beams are also shown in the figure. Note that above 30 eV there is excellent agreement with regard to peak positions among the three sets of curves shown in Fig. 5(a). At ~ 30 eV both experimental curves show a very small peak that is not seen in the theoretical calculation. The differences in the two experimental curves for $E \lesssim 20$ eV could be due to beam normalization problems. There is almost a factor of 2 difference between the two sets of measured absolute intensities at the peak maxima between 30–60 eV. The calculated absolute intensities in this region lie closer to the measurements of Demuth *et al.*[6]

Allowing the surface atoms to have a larger amplitude of vibration would decrease the peak intensities of the calculated curve somewhat. On the other

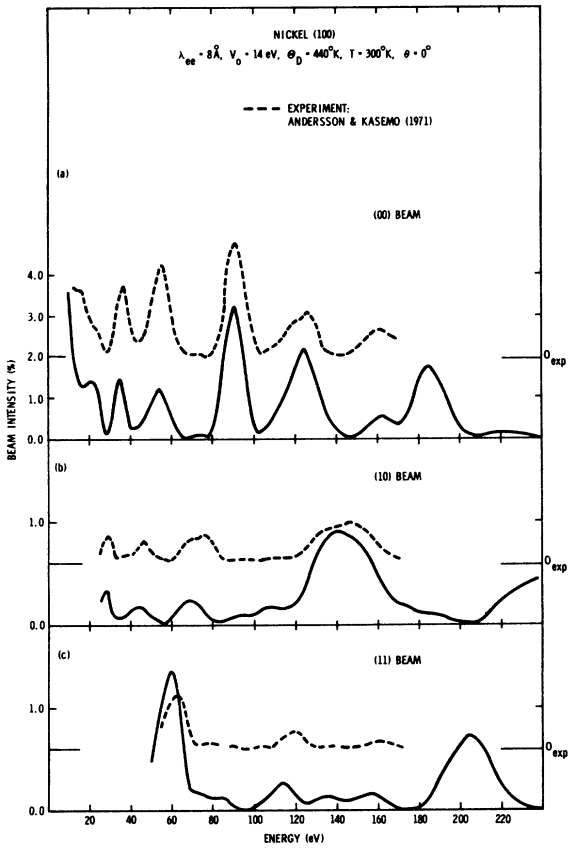

FIG. 4. Comparison between the predictions of the model calculations using $V_0 = 14$ eV and the experimental measurements of Andersson and Kasemo (Ref. 5). Except for the value of V_0, the details of the calculation and also of the experimental data are as detailed in Fig. 3.

hand, using a larger value of λ_{ee}—perhaps via an energy-dependent ImΣ—would increase the calculated peak intensities. In view of the differences in the measured absolute intensities between the two curves, it does not seem worthwhile to place too much emphasis on precisely matching the absolute intensities. In general, the agreement between the calculated and the measured intensity profiles is quite good. It is somewhat surprising that the model calculation describes the shape of the structure above 160 eV as well as it does using only five partial-wave components. At an electron energy of 160 eV (174 eV relative to the muffin-tin zero) the $l = 5$ phase shift has a value of about 0.18, which means that its effects should begin to appear. This may in part account for the lack of agreement with respect to the high-energy side of this structure.

A comparison between calculated intensity profiles and the experimental measurements of Demuth *et al.*[6] for $\phi = 0°$ and various angles of incidence is shown in Fig. 6. This azimuthal direction differs by 45° from that of Fig. 5. Particularly for $\theta = 7°$ there is excellent agreement between the calculated intensity profile and the experimental measurement with respect to both peak position and shape and also with respect to absolute intensities. At $\theta = 10°$ and 15° the agreement between theory and experiment, although somewhat less spectacular, is still quite respectable. The evolution of the profiles with increasing θ is adequately described by the model calculations. It is interesting to note that although there appears to be no noticeable energy dependence of the inner potential, there does appear to be a slight shift between the calculated and the experimental peaks that depends on θ. Qualitatively, the theoretical curve is about 2 eV higher than the experimental curve for $\theta = 7°$, it coincides with the experimental curve for $\theta = 10°$, and it is about 2 eV lower for $\theta = 15°$.

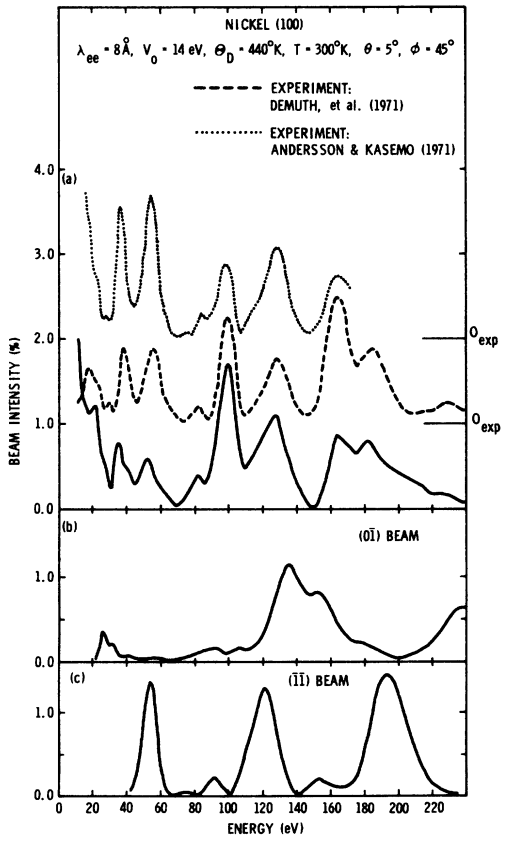

FIG. 5. Comparison between the predictions of the model calculations for the specular beam and the experimental measurements of Andersson and Kasemo (Ref. 5) and Demuth *et al.* (Ref. 6). Both the theoretical calculations and the experimental measurements are for the absolute reflectivity. The zero level has been shifted to the 1% mark for Demuth *et al.* and to the 2% mark for Andersson and Kasemo. Calculated intensity profiles for the (0$\bar{1}$) beam and the ($\bar{1}\bar{1}$) beam are shown in (b) and (c), respectively. The parameters used in the calculation are indicated in the figure.

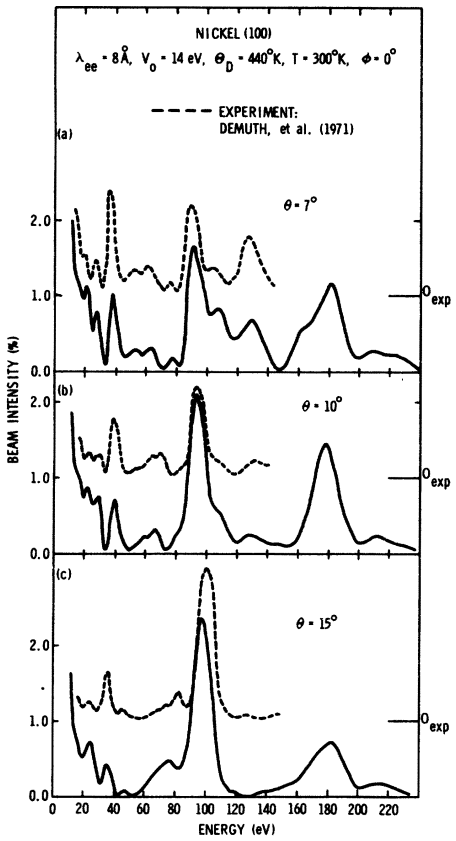

FIG. 6. Comparison between the predictions of the model calculations for the specular beam and the experimental measurements of Demuth *et al.* (Ref. 6) for $\phi = 0°$ and various angles of incidence. (a) shows the curves for $\theta = 7°$, (b) shows the curves for $\theta = 10°$, and (c) shows the curves for $\theta = 15°$. Both the theoretical calculations and the experimental measurements are for the absolute intensities. The zeros of the experimental curves have been shifted to the 1% mark. The parameters used in the calculation are indicated in the figure.

The origin of this drift is not clear at present. These same experimental curves are compared in Ref. 6 with model calculations based on Pendry's potential formulation.[10] The agreement between theory and experiment obtained in Ref. 6 is somewhat poorer than shown here. However, it must be pointed out that the calculations in Ref. 6 are based upon a perturbative approach and also use a different model for the electronic self-energy. A comparison of the perturbative approach with the method used in this paper is currently underway.[40]

Calculations of the intensity profiles for the $(0\bar{1})$ and $(\bar{1}\bar{1})$ beams for $\phi = 0°$ and $\theta = 7°$, 10°, and 15° are shown in Fig. 7. It is hoped that these calculations will motivate further experimental work that would provide additional tests of the model.

In general, the agreement between the theoretical calculations and the experimental measurements shown in Figs. 4–6 is satisfactory. However, one possible way that a clean metal surface may differ from the idealized model used in the calculations is in the layer spacing between the top two layers. To investigate the dependence of the calculated intensity profiles on this parameter, we write the upper layer spacing as

$$d' = (1+\gamma)d \,, \tag{14}$$

where d is the bulk layer spacing of 1.76 Å and γ denotes the deviation from the bulk value. Because of the generally good agreement between the experimental data and the calculated curves for $\gamma = 0$, we expect that for Ni(100) γ is quite small. Nevertheless it is important to try to place limits on it. In Fig. 8 we show calculated curves for $\gamma = -0.05$, 0, and 0.05 and compare them with the experimental data. These curves are for the specular beam at fairly small angles of incidence (where past experience indicates that the model calculations are most accurate) for both of the ex-

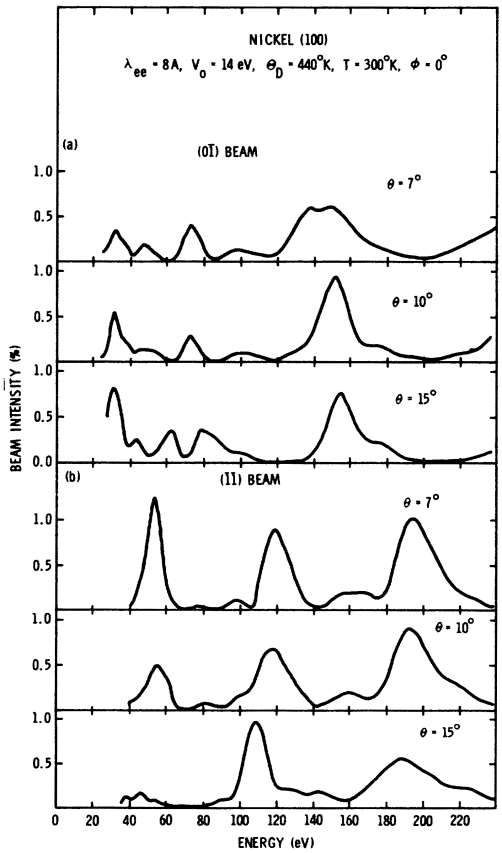

FIG. 7. Calculated intensity profiles for (a) the $(0\bar{1})$ beam and (b) the $(\bar{1}\bar{1})$ beam for $\phi = 0°$ and the indicated angles of incidence. The calculations are for the absolute intensity and use the parameters indicated in the figure.

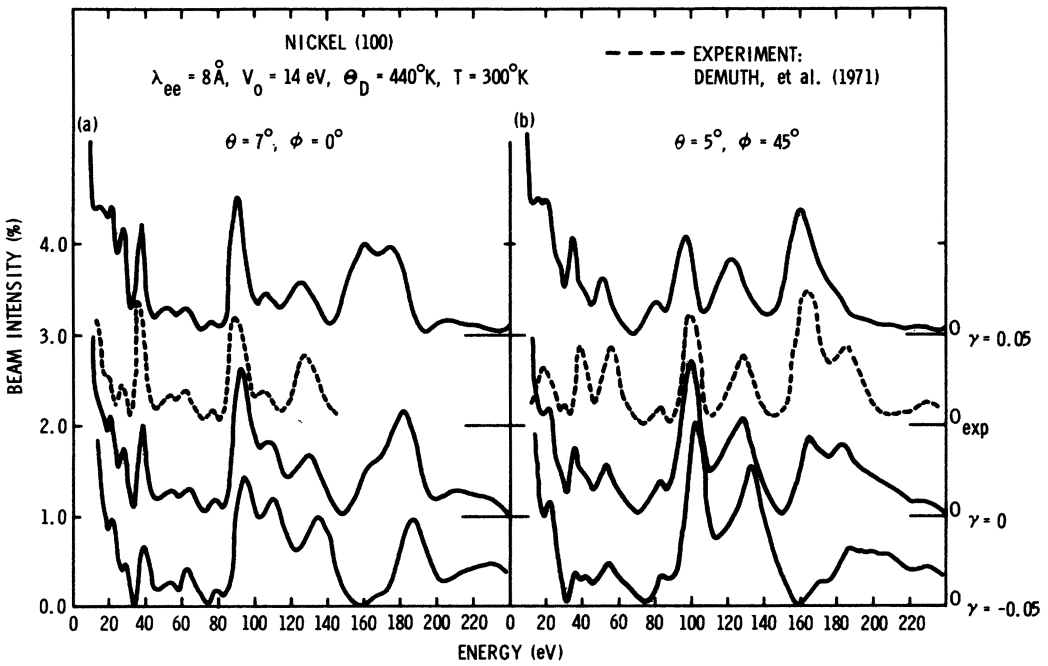

FIG. 8. Effect of a small change in the upper layer spacing on the calculated intensity profiles. The calculations are for the specular beam for $\theta = 7°$, $\phi = 0°$ in (a) and for $\theta = 5°$, $\phi = 45°$ in (b). Also shown as dotted lines are the corresponding measurements of Demuth *et al.* (Ref. 6). Both the theoretical and the experimental curves are for the absolute reflectivity with the theoretical calculations using the parameters indicated in the figure. The zero level has been shifted to the 1% mark for $\gamma = 0$, to the 2% mark for the experimental curves, and to the 3% mark for $\gamma = 0.05$. The upper layer spacing is defined in terms of γ through Eq. (14) of the text.

perimental azimuths. The experimental data of Demuth *et al.*[6] are also shown for ease of comparison. For the values $\theta = 7°$ and $\phi = 0°$ shown in Fig. 8(a), there is really not a great deal of difference between the various calculated curves over the energy range 10–150 eV covered by the experimental data. The experimental data do discriminate somewhat against the 5% contraction of the upper layer spacing. The most dramatic change is in the behavior of the calculated curves in the energy range >150 eV, for which there are no published experimental data at this azimuth. The calculated curves for $\theta = 5°$ and $\phi = 45°$ are shown in Fig. 8(b). Again the results below 150 eV appear to discriminate against a slight contraction of the upper layer spacing. A 5% expansion of the upper layer spacing pulls out the peak structure near 20 eV, resulting in a somewhat better agreement with the experimental data of Demuth *et al.*[6] However, in this energy range their data differ appreciably from those of Andersson and Kasemo[5] so the reliability of this diagnostic is unclear. Again the most pronounced difference between the calculated curves occurs for $E > 150$ eV. This agreement between the experimental curve and $\gamma = 0$ is clearly the best in this energy range.

A value of $\gamma = 0$ seems to provide a better description of the experimental data than $\gamma = \pm 0.05$, which provides limits on the value of d'. We thus conclude that the upper layer spacing for Ni(100) coincides with its bulk value to within ~0.1 Å. In view of the interdependence[3] between the profile changes for a given value of d' and the assumed values of $\lambda_{ee}(E)$, it does not seem reasonable to try to push the present model to a greater accuracy than this.

V. NICKEL (111)

In this section we consider experimental data consisting of absolute intensity measurements[8,9] for the specular beam at $T = 423$ °K and relative intensity measurements[7] for the nonspecular beams at $T = 300$ °K. Bulk thermal expansion[41] was taken into account by using a lattice constant of 3.526 Å for the $T = 423$ °K calculations. The same specular-beam-intensity data for Ni(111) is shown both in Refs. 8 and 9. However, in Ref. 8 the data are plotted as a function of momentum transfer not of electron beam energy as they are in Ref. 9. The experimental absolute intensity data shown here are taken from Ref. 9, but are plotted as a function of the polar angle measured from the surface normal, not the angle of incidence measured from

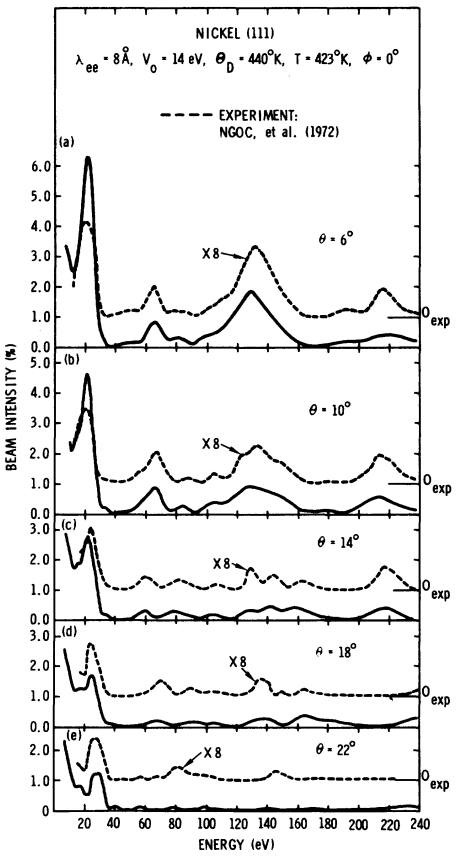

FIG. 9. Comparison between the predictions of the model calculations for the specular beam and the experimental measurements of Ngoc *et al.* (Ref. 9). The curves are labeled by the angle of incidence θ. Both the theoretical calculations and the experimental measurements are for the absolute intensities. The experimental intensities have been multiplied by 8 to place them on the same scale as the calculations and their zero levels have been shifted to the 1% mark. The parameters used in the calculation are indicated in the figure.

the surface plane was as done by Ngoc, Lagally, and Webb.[9] The data of Park and Farnsworth[7] were originally plotted as a function of $\cot\frac{1}{2}\theta$, where θ is the angle that the emerging beam makes with the surface normal. This variable has been converted back into beam energy in the present work.

In Fig. 9 we compare calculated intensity profiles for the specular beam with the experimental measurements of Ngoc *et al.*[9] One fact immediately stands out: Although there is a reasonable agreement between the model calculations and the experimental measurements with respect to peak positions and shapes (particularly for $\theta \leq 14°$), the absolute intensities differ by almost an order of magnitude. Since these data were taken at a higher temperature than that from Ni(100), one quickly notes that the effect of a larger amplitude of vibration for the surface atoms would be more pronounced in reducing the calculated intensity.[2,42] To gain some idea about the magnitude of this effect, the calculation for $\theta = 6°$ was redone using a value of $\Theta_D^S = 300$ °K to characterize the vibrational amplitude of the surface atoms. This gives the surface atoms about twice the mean-square vibrational amplitude of those in the bulk. The calculated curve, not shown in the figure, was quite similar in general appearance to the one using $\Theta_D^S = 440$ °K. The intensities of the peaks were reduced but not nearly enough to bring theory and experiment into correspondence, i.e., the intensity of the 23-eV peak was 5.6%, the intensity of the 68-eV peak was 0.65%, the intensity of the 131-eV peak was 1%, and the intensity of the 219-eV peak was 0.175%. Another way of reducing the calculated intensities would be to extend the onset of the damping beyond $\frac{1}{2}d$ from the outermost plane of surface atoms.[16] However, we know of no physical reason to expect this distance to be substantially different for the (100) and (111) faces. A stepped surface can have the effect of scattering intensity out of the region seen by the detector and thus reduce the measured intensity.[43,44] However, the experimental data do not exhibit the shifts in peak position and modulations of peak shape that accompany the intensity reduction.[43,44] We are thus unable to resolve the disagreement between the experimental and theoretical absolute intensities for the (111) face.

Looking at Fig. 9(a), we see that for $E > 200$ eV the theoretical peak is substantially broader than its experimental counterparts. Again we note that at an energy this high, the $l = 5$ partial-wave component probably needs to be taken into account for a reliable description of peak shape. Unlike the data from the (100) face, these data seem to show a slight energy dependence of the effective inner potential. This amounts to about 4 eV over a 200-eV range, which still is much less than electron-gas calculations predict.[34] The evolution of the intensity profiles with increasing θ is adequately described only up to $\theta = 14°$. For $\theta = 18°$ and 22° there is considerable deterioration of the agreement between theory and experiment. This deterioration of the agreement between theory and experiment is a fairly common occurrence,[3,11,12,15] and may be attributed at least in part to the oversimplified model of the electron-solid force law used in the calculations and to the assumption of an idealized planar surface. Experimental uncertainties in the azimuthal and polar angles of the incident beam may also be contributing to this effect.[45]

Model calculations of the $(\bar{1}0)$ and $(0\bar{1})$ beam intensities are presented in Fig. 10 for various

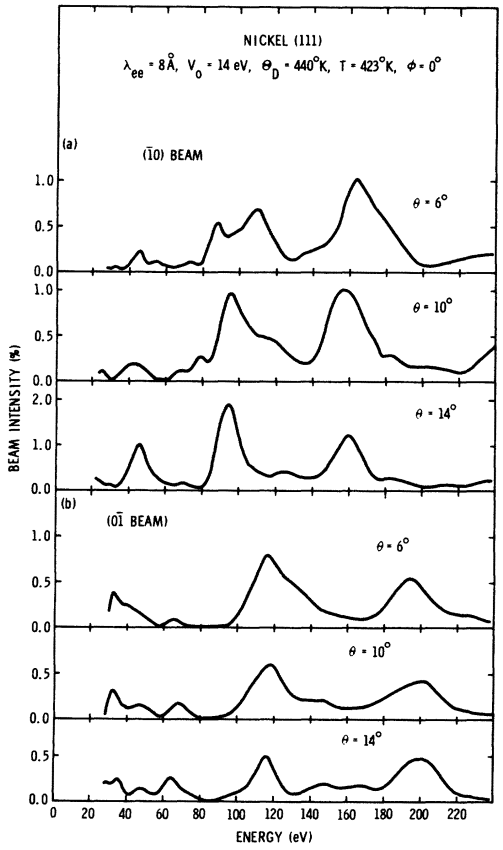

FIG. 10. Calculated intensity profiles for (a) the $(\bar{1}0)$ beam and (b) the $(0\bar{1})$ beam for the indicated angles of incidence. The calculations are for the absolute intensities and use the parameters indicated in the figure.

angles of incidence. Although Ngoc *et al.* [9] do not show any direct data for these beams, they do show "averaged" data at $T = 373$ °K. The largest peaks in these averaged data have intensities between 0.1 and 0.2%, which again is considerably smaller than the intensities of the prominent peaks in calculated curves.

Park and Farnsworth[7] give normalized relative intensity measurements for several nonspecular beams at normal incidence. These data are compared with the results of model calculations in Fig. 11, with the theoretical calculations and the experimental data being normalized at the first peak in the $(\bar{1}0)$ beam. The theoretical calculations give a good description of the intensity-profile variation from beam to beam. The experimental curves lie about 4 eV higher in energy than those in the model calculations. This takes the form of a constant offshift and does not indicate an energy dependence of the inner potential. The worst disagreement between theory and experiment occurs in the region above 190 eV for the (10) beam. Also additional "fine structure" is observed on the high-energy peaks in the $(\bar{1}0)$ and $(\bar{2}0)$ beams, which is not predicted theoretically. Using either a stronger potential (i.e., including the $l = 5$ partial-wave component) or a smaller value of $\mathrm{Im}\Sigma(E)$ in this region might tend to produce such additional structure.

We regard the comparison between theory and experiment shown in Figs. 9 and 11 as sufficient to argue for the basic validity of the model of the electron-solid force law used in the present work. To obtain limits on the deviation of the upper layer spacing of Ni(111) from its bulk value, calculations were again performed for different values of the upper layer spacing. The results of some of these are compared with experiment[9] in Fig. 12. The upper layer spacing is defined in terms of γ through Eq. (14), where $d = 2.0355$ Å for Ni(111)

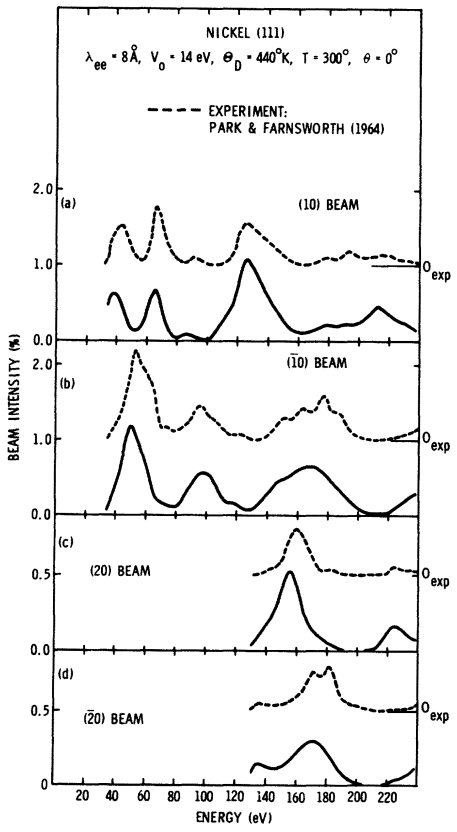

FIG. 11. Comparison between the predictions of the model calculations for the (10), $(\bar{1}0)$, (20), and $(\bar{2}0)$ beams at normal incidence and the experimental measurements of Park and Farnsworth (Ref. 7). The theoretical calculations are for the absolute intensities. The experimental measurements are only for the relative intensities. The two sets of curves have been normalized with respect to the first peak in the $(\bar{1}0)$ beam. The experimental zero levels have been shifted to the 1% mark for the (10) and $(\bar{1}0)$ beams and to the 0.5% mark for the (20) and $(\bar{2}0)$ beams. The parameters used in the calculations are indicated in the figure.

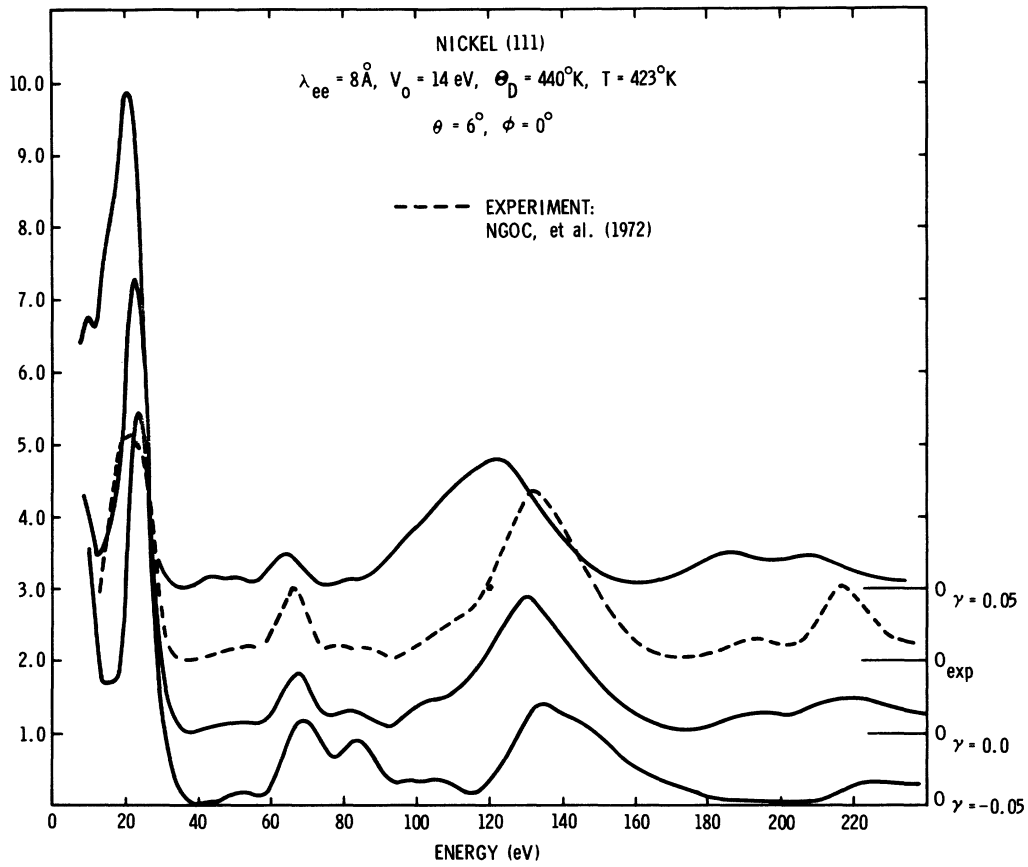

FIG. 12. Effect of a small change in the upper layer spacing on the calculated intensity profiles. The calculations are for the specular beam for $\theta = 6°$ and $\phi = 0°$. Also shown as the dotted line are the experimental measurements of Ngoc *et al.* (Ref. 9). Both the theoretical calculations and the experimental measurements are for the absolute intensities with the theoretical calculations using the parameters indicated in the figure. The experimental curve has been multiplied by a factor of 8 to place it on the same scale as the calculations. The zero level has been shifted to the 1% mark for $\gamma = 0$, to the 2% mark for the experimental curve, and to the 3% mark for $\gamma = 0.05$. The upper layer spacing is defined in terms of γ through Eq. (14) of the text.

at $T = 423\,°K$. The calculated intensity profile for $\gamma = 0$ agrees considerably better with the experimental measurement than the calculated curves for an expanded or a contracted upper layer spacing. We thus conclude that the upper layer spacing for Ni(111) coincides with its bulk value to within ~ 0.1 Å. For the reasons given at the end of Sec. IV, it does not seem sensible to try to push the present model to a greater accuracy than this.

VI. SUMMARY AND CONCLUSIONS

In this paper we used a finite-temperature version[1-4] of the inelastic collision model to analyze experimental low-energy-electron-diffraction intensity profiles[5-9] for Ni(100) and Ni(111). Some minor modifications of the previous computational technique[3] that have proven useful were detailed in Sec. II. Two of these modifications—(i) a change to a "real" spherical-harmonic basis set and (ii) a change in the algorithm to calculate the effective electron–ion-core elastic scattering vertex—were simply for computational convenience. The inclusion of electronic self-energy renormalization effects beyond the position of the surface ion cores contains some physics in that it accounts phenomenologically for the extension of the electron cloud beyond the surface ion cores[6,11,14,23] and also in part for energy losses to surface plasmons while the electron is still outside the solid.[16,27] The particular choice of surface boundary conditions used and the rationale behind it were also discussed.

The electron–ion-core model potential used in this work was constructed using conventional band-structure techniques without modifying[10] the exchange approximation for the high-energy range of LEED. The inner potential was determined independently of the LEED data by fitting the position of the d-wave resonance to work-function measurements.[17] The imaginary part of the one-electron

self-energy was parametrized using a constant mean free path and the effects of the lattice vibrations parametrized using an effective Debye temperature.

The model calculations adequately described *both* the absolute intensities and the shapes of the intensity profiles for Ni(100). This would seem to indicate that the model contains the essential physics of the problem. However, previous work on aluminum using the same basic model yielded calculated intensities that were considerably higher than those experimentally measured, [46] although there was good correspondence with respect to the shapes of the intensity profiles. This problem also occurred here for Ni(111), where the model gave an adequate description of the shapes of the experiment intensity profiles but not their absolute intensities. Assuming that the experimental measurements really are for the current per unit area reflected into a given beam divided by the incident current per unit area as defined in Eq. (2.22) of Ref. 3, and that the faces in question are reasonable approximations to chemically clean idealized surfaces, we find this degree of variation from face to face of the same material especially puzzling. To obtain limits on the upper layer spacing, the dependence of the calculated intensity profiles on this parameter was investigated. We conclude that to within ~0.1 Å the upper layer spacing coincides with its bulk value for both faces.

Note added in proof. Recently Demuth (private communication) has made absolute LEED intensity measurements for Ni(111). Both the shapes of his intensity profiles and their absolute magnitudes are i good agreement with the calculations presented her Hence it appears that the problem in comparing the absolute intensities between the (100) and (111) face mentioned in this paper is due to different "absolut normalization procedures" used by different experimental groups. I would like to thank J. E. Demuth for making his work available to me prior to publication.

ACKNOWLEDGMENTS

I should like to thank Dr. R. L. Park for helpful discussions regarding nickel surfaces and D. G. Schreiner for his assistance in plotting the experimental data.

---

*Work supported by the U.S. Atomic Energy Commission.

[1]C. B. Duke and G. E. Laramore, Phys. Rev. B **2**, 4765 (1970).

[2]G. E. Laramore and C. B. Duke, Phys. Rev. B **2**, 4783 (1970).

[3]G. E. Laramore and C. B. Duke, Phys. Rev. B **5**, 267 (1972).

[4]C. B. Duke, D. L. Smith, and B. W. Holland, Phys. Rev. B **5**, 3358 (1972).

[5]S. Andersson and B. Kasemo, Surf. Sci. **25**, 273 (1971).

[6]J. E. Demuth, S. Y. Tong, and T. N. Rhodin, J. Vac. Sci. Technol. **9**, 639 (1972).

[7]R. L. Park and H. E. Farnsworth, Surf. Sci. **2**, 527 (1964).

[8]M. G. Lagally, T. C. Ngoc, and M. B. Webb, J. Vac. Sci. Technol. **9**, 645 (1972).

[9]T. C. Ngoc, M. G. Lagally, and M. B. Webb, Surf. Sci. 35, 117 (1973).

[10]J. B. Pendry, J. Phys. C **2**, 1215 (1969).

[11]D. W. Jepsen, P. M. Marcus, and F. P. Jona, Phys. Rev. Lett. **26**, 1365 (1971).

[12]D. W. Jepsen, P. M. Marcus, and F. P. Jona, Phys. Rev. B **5**, 3933 (1972).

[13]P. M. Marcus, D. W. Jepsen, and F. P. Jona, Surf. Sci. **31**, 180 (1972).

[14]D. W. Jepsen, P. M. Marcus, and F. P. Jona, Phys. Rev. B **6**, 3684 (1972).

[15]G. E. Laramore and A. C. Switendick, Phys. Rev. (to be published).

[16]C. B. Duke, N. O. Lipari, and U. Landman, Phys. Rev. (to be published).

[17]L. W. Swanson and R. W. Strayer, J. Chem. Phys. **48**, 2421 (1968).

[18]This is the value of the bulk Debye temperature used in Ref. 5. X-ray measurements give a value of $\Theta_D = 410 \pm 10$ °K [R. H. Wilson, E. F. Skelton, and J. L. Katz, Acta Crystallogr. **21**, 635 (1966)]. Elastic constants obtained from Young's modulus give a value of $\Theta_D = 445$ °K (F. H. Herbstein, Adv. Phys. **10**, 313 (1961)]. The difference between these values of Θ_D is not crucial to the present work.

[19]C. B. Duke and W. W. Tucker, Jr., Surf. Sci. **15**, 231 (1969); Phys. Rev. Lett. **23**, 1163 (1969).

[20]A. U. MacRae and L. H. Germer, Ann. Phys. (N.Y.) **101**, 627 (1963).

[21]See, for example, Fig. 14 of Ref. 3.

[22]See, for example, J. D. Jackson, *Classical Electrodynamics* (Wiley, New York, 1963), Sec. 3.4.

[23]S. Y. Tong, T. N. Rhodin, and R. H. Tait, Phys. Rev. (to be published).

[24]If the electronic self-energy is assumed to be spherically symmetric, then taking its momentum dependence into account merely involves including a quasiparticle renormalization factor at each wave-vector integration. See Ref. 23 for a discussion of this point.

[25]G. E. Laramore, Phys. Rev. B **6**, 1097 (1972).

[26]G. E. Laramore, Phys. Rev. B **6**, 2950 (1972).

[27]P. J. Feibelman, C. B. Duke, and A. Bagchi, Phys. Rev. B **5**, 2436 (1972); A. Bagchi and C. B. Duke, Phys. Rev. B **5**, 2784 (1972); P. J. Feibelman, Surface Sci. (to be published).

[28]See, for example, F. P. Jona, IBM J. Res. Dev. **14**, 444 (1970).

[29]D. Liberman, J. T. Waber, and D. T. Cromer, Phys. Rev. **137**, 27 (1965).

[30]T. Loucks, *Augmented Plane Wave Method* (Benjamin, New York, 1967).

[31]J. C. Slater, Phys. Rev. **81**, 385 (1951).

[32]W. Kohn and L. J. Sham, Phys. Rev. **140**, 1133 (1965).

[33]J. E. Houston, R. L. Park, and G. E. Laramore Phys. Rev. Lett. 30, 846 (1973).

[34]A. C. Switendick (private communication).

[35]The idea of using the d-wave resonance to locate the center of gravity of the d band also occurs in the renormalized-atom approach of L. Hodges, R. E. Watson, and H. Ehrenreich, Phys. Rev. B **5**, 3953 (1972).

[36]J. C. Riviere, Solid State Surface Sci. **1**, 179 (1969); N. D. Lang and W. Kohn, Phys. Rev. B **3**, 1215 (1971).

[37]See, for example, L. Hedin and S. Lundquist, in *Solid State*

Physics, edited by F. Seitz, D. Turnbull, and H. Ehrenreich (Academic, New York, 1969), Vol. 23.
[38]S. Andersson and J. B. Pendry, J. Phys. C **5**, L41 (1972).
[39]S. Y. Tong (private communication).
[40]S. Y. Tong, G. E. Laramore, and T. N. Rhodin (unpublished).
[41]See A. Goldsmith, T. E. Waterman, and H. J. Hirschhorn, *Handbook of Thermophysical Properties of Solid Materials* (MacMillan, New York, 1961), Vol. I, p. 459.
[42]C. B. Duke, G. E. Laramore, B. W. Holland, and A. M. Gibbons, Surf. Sci. **27**, 523 (1971). See, in particular, Fig. 10.
[43]G. G. Laramore, J. É. Houston, and R. L. Park, J. Vac. Sci. Technol. **10**, 196 (1973).
[44]J. E. Houston, G. E. Laramore, and R. L. Park, Surface Sci. **34**, 477 (1973).
[45]J. M. Baker and J. M. Blakely, Surface Sci. **32**, 45 (1972).
[46]J. M. Burkstrand, Ph.D. thesis (University of Illinois, 1972) (unpublished); Phys. Rev. B **1**, 3443 (1973).

PHYSICAL REVIEW B VOLUME 8, NUMBER 2 15 JULY 1973

Magnetic Breakdown and Phase-Coherent Galvanomagnetic Effects

C. E. T. Gonçalves da Silva* and L. M. Falicov
Department of Physics,† University of California, Berkeley, California 94720
(Received 22 December 1972)

This paper presents a generalization of Pippard's network-model approach for the calculation of transport properties in metals in the presence of magnetic breakdown and partial phase coherence of the wave function. The generalization consists of introducing an ensemble of equivalent networks characterized by a well-defined fully coherent finite system of orbits. It allows for relatively easy computation of the transport effective path in the infinite-relaxation-time approximation. The idea is applied to two specific examples: the linear chain and the hexagonal network; the latter can be considered a good model for magnesium and can be compared with existing and future experiments.

I. INTRODUCTION

The aim of this paper is to present a model calculation of phase-coherence effects on the transport properties of systems in which magnetic breakdown is present. It is now over a decade since the existence of the phenomenon of magnetic breakdown (MB)—the interband tunneling of electrons in the presence of a strong magnetic field—has been recognized.[1] In this decade the experimental studies[2] have not only decisively confirmed the existence of the phenomenon, but also the quality of the data has by far surpassed the limits of the existing theoretical analyses. In the presence of MB, oscillations in the magnetoresistance have been observed which are caused by quantum effects distinct from the density-of-states oscillations that are observed in the de Haas–van Alphen or Shubnikov–de Haas effects.[2,3] We can gain a qualitative understanding of these new effects if we consider the semiclassical picture of electrons moving along well-defined trajectories.[4] When MB is operative, the electron may choose between different paths in moving from a given initial position to a given final position. This multiplicity of paths indicates that in a quantum treatment, observable interference effects should be present, *as long as the electronic wave function maintains its coherence along the various paths between given initial and final points*. As Pippard[5] has shown, the parameter that governs the coherence length is the density of dislocations in the crystal. In a crystal with a very high density of dislocations, the coherence length is negligible, no interference effects are present, and the transport properties, as calculated from the Boltzmann equation, reproduce the general features of the experimental result.[6] As the density of dislocation is reduced, the coherence length increases and the first oscillations in the magnetoresistance, coming from paths that encircle the smallest areas, begin to appear. This regime has been successfuly treated by Falicov *et al.*[7] If we try to improve on their approach there are two ways to go: we can either do quantum transport theory starting from a suitable approach, e.g., Kubo's formula, or we can adopt a more modest, but *ad hoc* scheme for calculation of the conductivity based on semiclassical, e.g., Pippard's network, models.[8] The advantages and disadvantages of both methods are quite clear. It we use the quantum transport approach, we have, to begin with, a well-defined theory for which, in principle, suitable approximation schemes could be devised. So far, however, nobody has succeeded in tackling the difficulties involved in such an approach.[9,10] If, on the other hand, we start from the network model, we step into a vacuum, so to speak. The problem is not completely well-defined and we must depend to some degree on intuition. Although the network model has been amply discussed in the literature and *ad hoc* justi-